COBEM 2021 26th International Congress of Mechanical Engineering
November 22-26, 2021, Virtual Congress, Brazil

COB-2021-0301
REDUCED ORDER MODELING BASED ON COMPUTATIONAL FLUID DYNAMICS: A STUDY OF CASE FOR A STIRRED TANK

Alexandre M. S. Costa
Departamento de Engenharia Mecânica, Universidade Estadual de Maringá, Av Colombo 5790, Maringá, PR, Brasil
amscosta@uem.br

Marcelo José Alba
Departamento de Física, Universidade Tecnológica Federal do Paraná, R Marcilio Dias 635, Apucarana, PR, Brasil
marceloalba@utfpr.edu.br

Abstract. *Progresses in hardware computational power and numerical algorithms had expanded the class of industrial flows that can be approached by Computational Fluid Dynamics methods. In recent years, Reduced Order Modeling (ROM) had been applied extensively in engineering problems tackled by Computational Fluid Dynamics. Reduced Order Methods derives on splitting a higher order problem in two steps: a computational expensive, comprising CFD runs; and a less expensive, comprising ROM object generation and consumption. The ROM consumption task can also be performed in a simpler hardware platform or integrated in a full multiscale model of an industrial plant (digital twin).In this work is applied the ROM workflow for a laboratory scale stirred tank CFD model. The practical implementation of the ROM to estimate the relationship between rotation velocity and fluid properties is explained in detail. Computational fluid dynamics (CFD) verification runs are used to assess the reliability of the reduced-order model. Findings indicate that the ROM is capable of predicting the mixer performance for a wide range of input conditions.*

Keywords: *Reduced Order Modeling, CFD, digital twin, stirred tank*

1. INTRODUCTION

The use of Reduced Order Modeling (ROM) combined with the computational fluid dynamics (CFD) results had expanded in the last decades. Without being exhaustive, we can cite applications in fields as diverse as hemodynamics (Ballarin, *et al.*, 2015; Ballarin *et al.*, 2016; Han *et al.*, 2020; Biancolini, *et al.*, 2020), energy conversion (Lang *et al.*, 2009; Zhong *et al.*, 2020) and aeronautics (Jung *et al.*, 2011). For a more in-depth discussion of applications c.f. Rozza *et al.* (2018).

From a mathematical point of view, the generation of reduced order models uses diversified methodologies (c.f. Chinesta *et al.*, 2014; Hesthaven, *et al.*, 2016; Xiao *et al.*, 2015; Haasdonk and Ohlberger, 2008; Stabile *et al.*, 2017; Stabile and Rozza, 2018). In general terms, ROM generation starts with learning the physics of a given model (Maquart *et al.*, 2020). The learning set includes a set of parameterized CFD solutions generated following a Design of Experiments methodology (Montgomery, 2013; Almeida *et al.*, 2020). Once generated, the ROM can be identified as a digital object, which can be used with reduced computational cost (Quarteroni and Rozza, 2014). In this way, an approximation of the field of CFD solutions for any variable becomes available almost in real-time. The availability of a field of solutions by ROM techniques distinguishes them from response surface methods applied to CFD solutions since the latter are characterized by the generation of functional correlations between a set of input parameters and a set of output parameters (Myers, *et al.*, 2016). Another advantageous feature of the ROM object is the possibility of integration with one-dimensional process models, embedded hardware systems, and digital twins (Laubenbacher, *et al.* 2021).

With the emergence and improvement of computational techniques and tools, the studies of stirred tank mixers through CFD gained importance in the end of the last century. (Bakker and Fasano, 1993; Armenante *et al.*, 1997; Brucato *et al.*; 1998). Since then, among others, more specific studies have been carried out, such as mixing time (Shekhar e Jayanti, 2002; Rodgers *et al.*, 2011), drag and turbulence models (Alexopoulos *et al.*, 2002; Wadnerkar *et al.*, 2012; Tamburini at al., 2014), mixtures of liquids and solids (Kee and Tan, 2002; Blais and Bertrand, 2017; Wang *et al.*, 2017).

In this work, the application of the ROM technique was investigated for the prediction of velocity solution fields ($\overline{V}$), kinetic energy (k) e specific turbulent dissipation (ω) in an existing mixer, shown in Figure 1. This is a lab-scale stirred tank with a four-blade impeller and four baffles on the tank wall. Although there is a large number of stirred tank models with different specificities for each industrial use, the model presented was chosen due to its versatility of use and reproducibility with CAD and CFD software.

(a) (b)

Figure 1. (a) Side view and (b) front view of the mixer (Moro, 2016).

2. METODOLOGY

The ROM construction method uses the singular value decomposition technique (Carlberg *et al.*, 2013) of variable's fields obtained from CFD solutions. Initially, a vector base for the solution field of variable X is built. Such base is dependent on the selected input parameters. The construction follows Eq. (1).

$$M = U\Sigma V^{*} \tag{1}$$

In the previous equation, M is the matrix of singular values, whose columns are composed of the solution fields of the variable X for several values of the input parameters. These columns are called learning snapshots. The Σ is a diagonal matrix, whose elements $\sigma_0,...,\sigma_n$ are called singular values. In Eq. (1) U and V are unit matrices, where the columns of U and V are composed respectively of the left singular vectors U_i and the left singular vectors V_i of the matrix M.

In the next step, the solution field of the variable X is approximated as a linear combination of r vectors U_i, by means of Eq. (2).

$$X = \sum_{i=1}^{r} \alpha_i U_i \tag{2}$$

The α_i interpolation coefficients are approximated by the genetic aggregation meta-model (Viana *et al.*, 2009; Acar, 2010; Ben Salem and Tomaso, 2018). The ROM construction method described above is implemented in the ANSYS Design Explorer 2021R1 software used in this study.

Figure 2(a) illustrates the geometry and coordinate system used as a starting point for CFD simulations. To simulate the rotating domain, the moving reference frame (MRF) approach was used. To reduce the computational cost, a quarter-domain periodicity was adopted (see Figure 2(b)). Thus, the number of polyhedral cells generated in the ANSYS Meshing 2021R1 software was constituted of 88221 cells for the rotating part (green figure), and 28895 cells for the stationary part (blue figure). As this refinement level is considered adequate (Moro, 2016), no further mesh refinement was done.The standard k-ω turbulence model was adopted. The CFD solver used was pressure-based and with coupled equations (PBCS), available in ANSYS Fluent 2021R1 software. The pseudo-transient approach was also adopted with explicit relaxation factors of 1, 1, 0.75, 0.5, 0.5 (density, turbulent kinetic energy, specific turbulent kinetic energy dissipation, momentum, pressure). The spatial discretization scheme was second-order upwind for pressure, momentum, turbulent kinetic energy, and specific dissipation of turbulent kinetic energy.

For the construction of the ROM summarized by Eq. (1) and (2), several CFD simulations were generated. For such learning simulations, the input parameters could vary in the following ranges: blade rotation speed ϕ (40-400 rad/s); fluid density ρ (1000-1400 kg/m^3) and its viscosity μ (10^{-3}-10^{-2} kg/(m.s)). Accordingly, it is emphasized that permitted ranges of variation of parameters followed the actual limits of rotation (Moro, 2016); and the density and viscosity to aqueous solutions (Melinder, 2010).

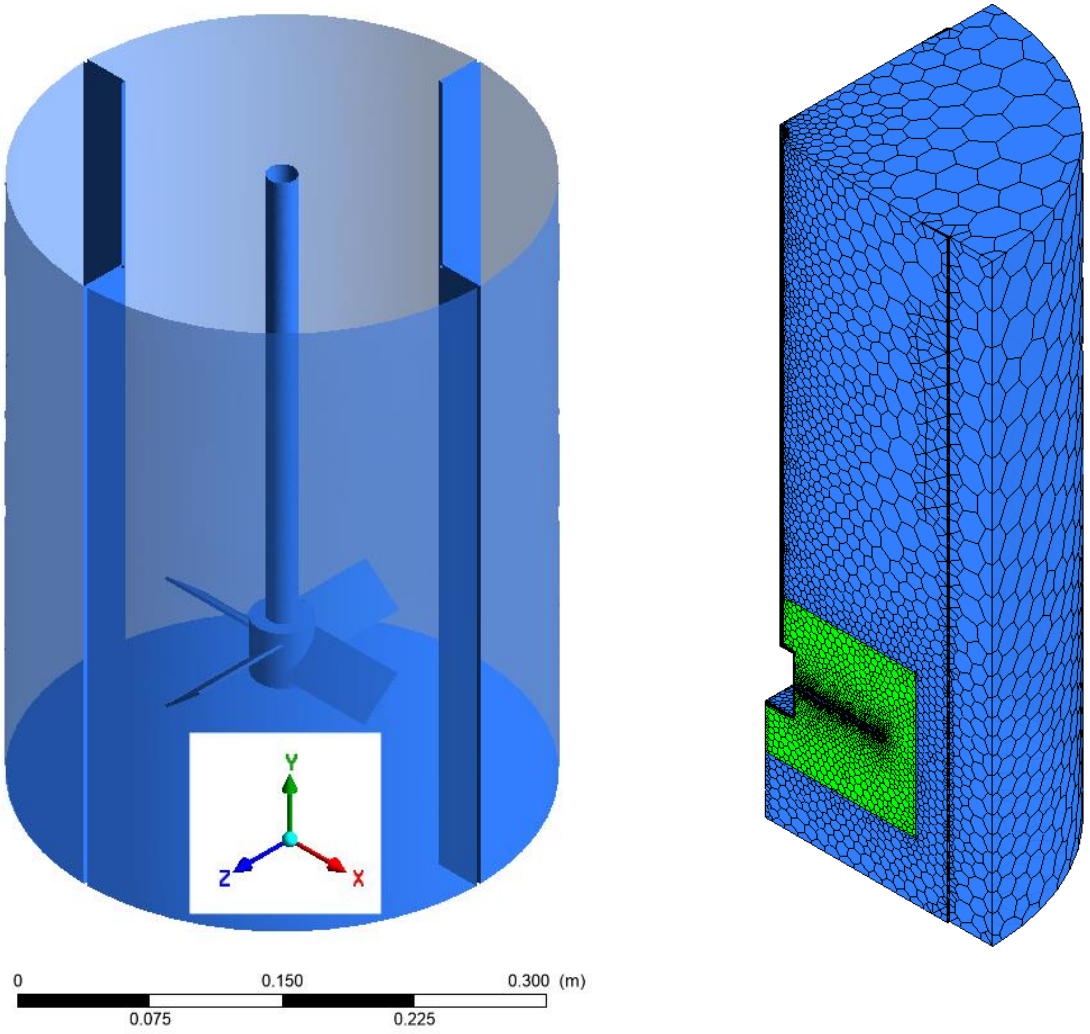

(a) (b)

Figure 2. (a) Mixer geometry and (b) polyhedral mesh for a quarter domain

3. RESULTS AND DISCUSSION

Table 1 presents the values of the input parameters for the learning CFD simulations. Values were generated using the Optimal Space-Filling algorithm (Antony, 2013).

Table 1. Summary of learning points for ROM generation.

Learning point #	ϕ (rad.s^{-1})	ρ (kg.m^{-3})	μ (kg m^{-1} s^{-1})	**Learning point #**	ϕ (rad.s^{-1})	ρ (kg.m^{-3})	μ (kg m^{-1} s^{-1})
1	227.5	1175	0.0026875	13	182.5	1358	0.0030625
2	317.5	1075	0.0019375	14	107.5	1325	0.0083125
3	122.5	1258	0.0015625	15	47.5	1158	0.0038125
4	257.5	1242	0.0060625	16	332.5	1375	0.0041875
5	212.5	1225	0.0098125	17	302.5	1292	0.0011875
6	362.5	1092	0.0053125	18	272.5	1042	0.0079375
7	77.5	1308	0.0049375	19	167.5	1125	0.0056875
8	377.5	1208	0.0034375	20	287.5	1342	0.0085875
9	152.5	1108	0.0094375	21	197.5	1392	0.0064375
10	62.5	1192	0.0075625	22	347.5	1142	0.0090625
11	242.5	1008	0.0045625	23	392.5	1275	0.0071875
12	92.5	1025	0.0068125	24	137.5	1058	0.0023125

In Figure 3 is presented one sample of the magnitude of the velocity field generated from the ROM object. As mentioned before, the generation of a spatial field of variables, using arbitrarily selected input parameter values (within the range of learning simulations) is one of the main advantages of the ROM technique.

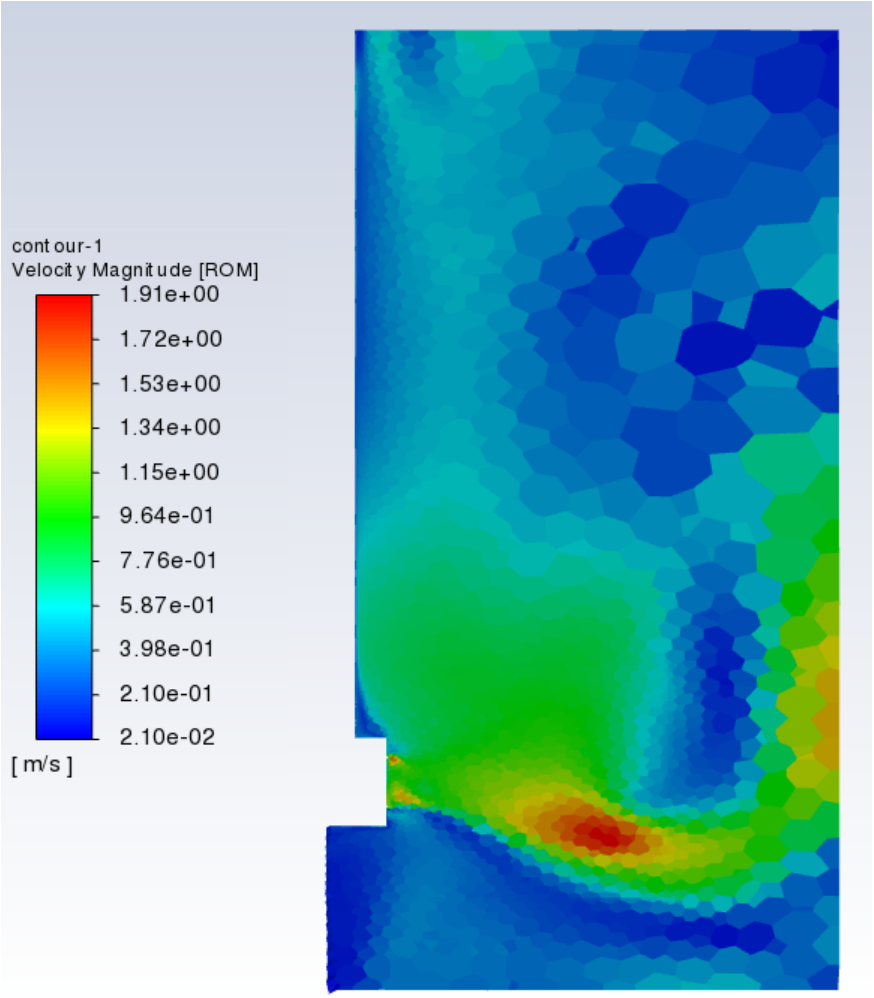

Figure 3. Velocity magnitude surface contour in a plane at 45º, derived from ROM results (ϕ = 40 rad/s, ρ = 1400 kg/m^3, μ = 5.5 10^{-3} kg/(m s)).

The access of fields values quality predicted by the ROM technique is done through several metrics. Such metrics are applicable to both learning simulations (snapshots) and verification CFD simulations. The addition of more simulation points (refinement points) or the inclusion of verification points in the set of learning simulations are strategies that can be considered to improve the quality metrics of the ROM object.

The metric L^{∞}_{error}, called L-infinity norm, is associated with the error defined in Eq. (3):

$$L^{\infty}_{error} = \max_{j=1...N} \left| Y_{i,j} - Y_{i,j} \right| \tag{3}$$

In the previous equation: Y_i corresponds to the variable field obtained for the i-th CFD solution; N corresponds to the size of the snapshot; $Y_{i,j}$ corresponds to the j-th value of the variable field obtained by CFD solution for the i-th snapshot; and $Y_{i,j}$ corresponds to the ROM approach to this j-th value

The metric $L^{2}_{error}\left(Y_i\right)$, called norm-2 error, is associated with the absolute error defined in Eq. (4):

$$L^2_{error}\left(Y_i\right)=\sqrt{\sum_{j=1}^{N}\left(Y_{i,j}-Y_{i,j}\right)^2} \tag{4}$$

To define the relative error, the metric used is $L^2\left(Y_i\right)$, called L2-norm, defined in Eq. (5).

$$L^2\left(Y_i\right)=\sqrt{\sum_{j=1}^{N}Y_{i,j}^2} \tag{5}$$

Thus, the relative error associated with the i-th snapshot $L^2_{relative-error}\left(Y_i\right)$, based on the L2-norm, is given by:

$$L^2_{relative-error}\left(Y_i\right)=\frac{L^2_{error}\left(Y_i\right)}{\frac{1}{S}\sum_{k=1}^{S}L^2\left(Y_k\right)} \tag{6}$$

In the previous equation, the S index corresponds to the number of learning points (snapshots) or the number of verification points, respectively.

Figure 4 presents a histogram of the distribution of L^{∞}_{error} errors between the ROM approach and the learning (snapshots) and verification simulations.

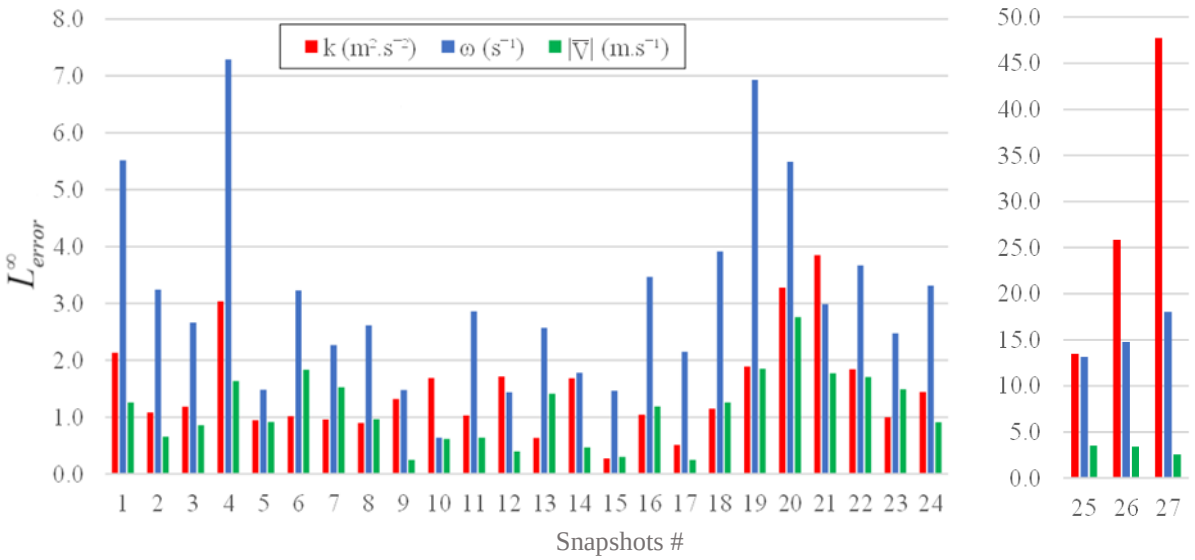

(a) (b)

Figure 4. L^{∞}_{error} absolute errors to ROM approach: (a) learning points and (b) verification simulations (The ω values were multiplied by 10^{-4})

The analysis of Figure 4(a) and (b) indicates that the errors associated with the verification points are always greater than the errors associated with the learning points. For verification points, the smallest errors are associated with velocity fields. In turn, in figure 4(a) the errors associated with velocity fields were generally smaller or of similar order of magnitude of the turbulent kinetic energy errors. The higher values associated with the turbulent kinetic energy dissipation field should also be highlighted.

Figure 5 presents a histogram of the distribution of errors $L^2_{relative-error}\left(Y_i\right)$ between the ROM approach and the learning and for the verification points.

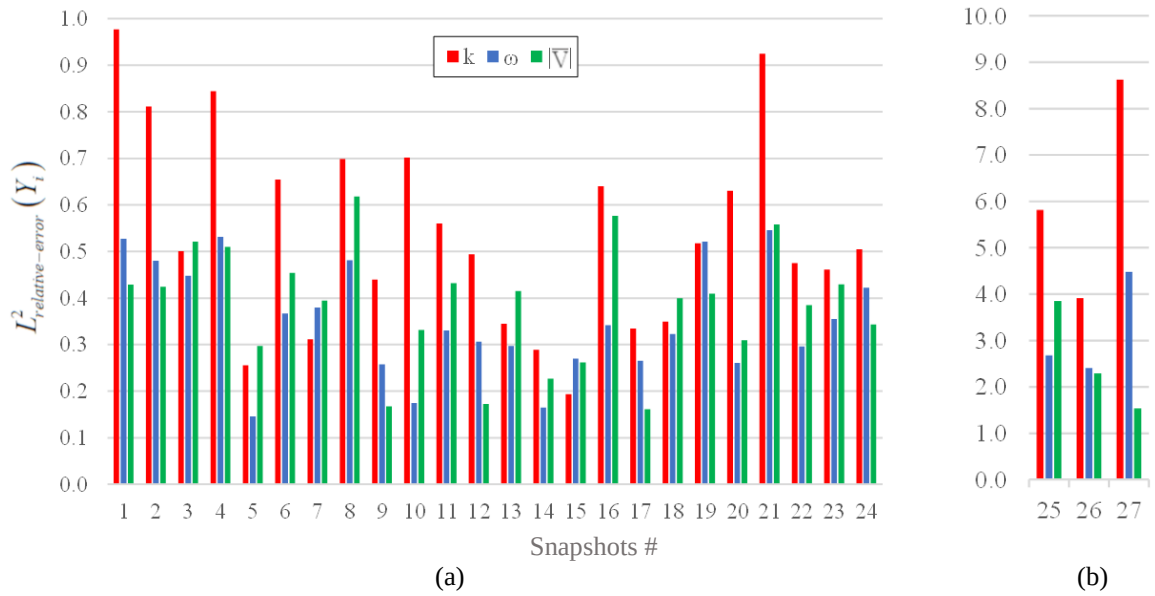

Figure 5. $L^2_{relative-error}(Y_i)$ percentual relative errors in the ROM approach: (a) learning points and (b) verification simulations.

The analysis of Figure 5(a) and (b) shows again the more favorable values of the error associated with the learning points when compared to the verification points. The maximum error level of 1% for learning points and around 8.7% for verification points is also highlighted. The analysis of the figures also indicates that the percentage errors associated with turbulent kinetic energy fields were located in the largest ranges, followed by errors associated with turbulent kinetic energy velocity and dissipation fields.

Figures 4 and 5 also show the degree of non-uniformity for the level of the error for all snapshots and which snapshots have the highest and lowest errors.

The cumulative distribution error is show in Figures 6 and 7, which allows quickly see what percentage of snapshots have an error smaller than a given value.

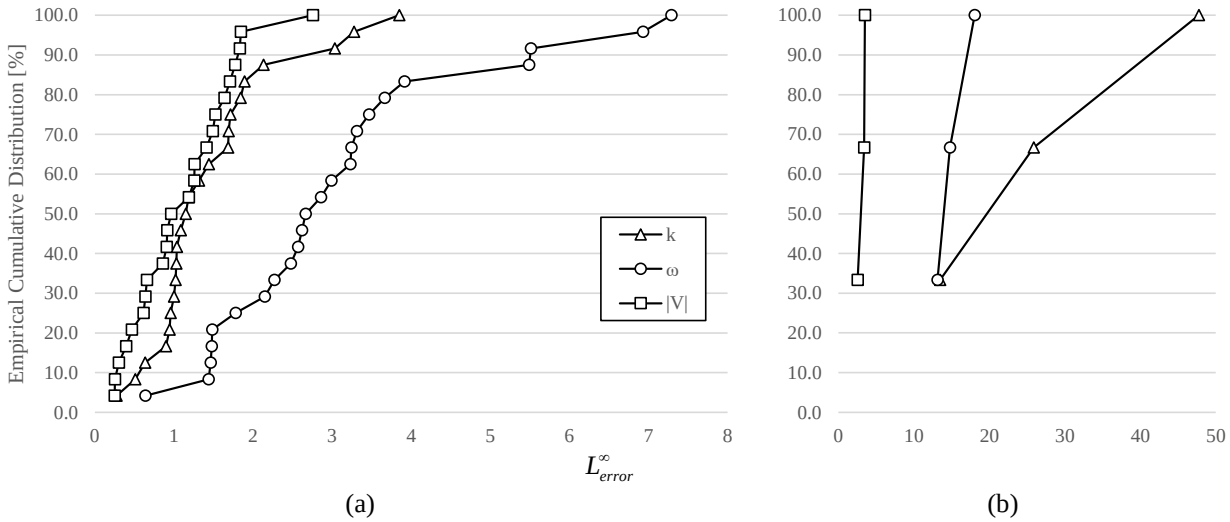

Figure 6. Empirical cumulative distributions of L^{∞}_{error} absolute errors: (a) learning points and (b) verification simulations (The ω values were multiplied by 10^{-4}).

The slope of the curves in Figure 6(a) demonstrates a more abrupt growth trend of the absolute error L^{∞}_{error} in the last snapshots of the learning points. As for the snapshots of the verification simulations, only the kinetic energy presented a more expressive error growth.

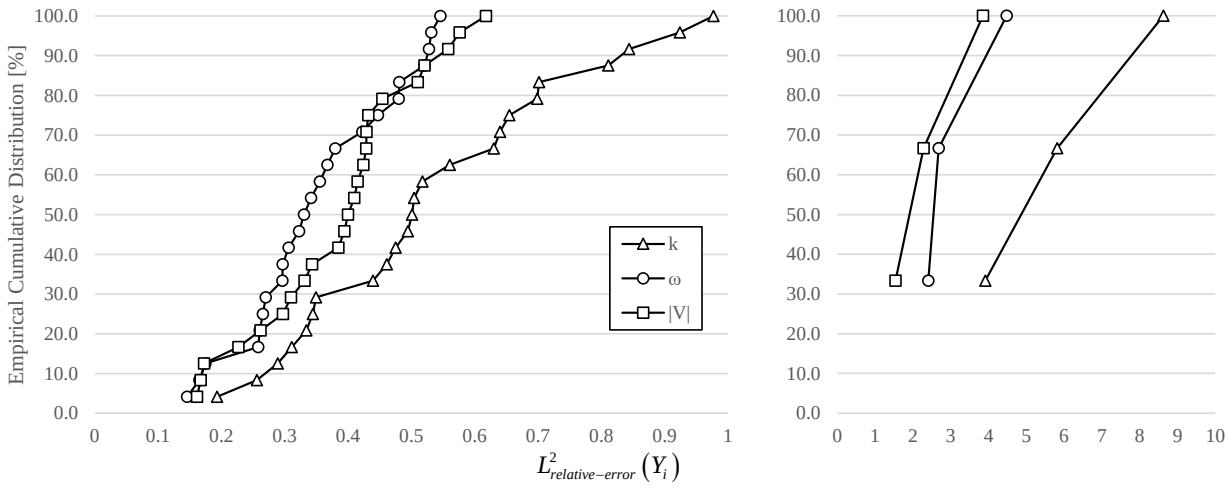

Figure 7. Empirical cumulative distributions of $L^2_{relative-error}(Y_i)$ percentual relative errors: (a) learning points and (b) verification simulations.

On the other hand, the slope of the cumulative $L^2_{relative-error}(Y_i)$ relative error curves in Figure 7(a) show a more linear growth trend without the steep slope shown in the absolute errors in Figure 6(a), that is, of the learning points. In the case of verification simulation snapshots, we also noticed the maintenance of more expressive errors for kinetic energy, with a very similar behavior for ω and $|\bar{V}|$.

Table 2 summarizes the ROM goodness of fit considering the errors associated with the whole snapshot and verification sets, for the three variable fields considered in this study.

Table 2. ROM Fit Quality

Errors	**Velocity ($\|\bar{V}\|$)**	**Specific Dissipation Rate (ω)**	**Turbulent Kinetic Energy (k)**
$L^2_{global-error} = \frac{\sqrt{\sum_{i=1}^{S}\left[L^2_{error}(Y_i)\right]^2}}{\sqrt{\sum_{i=1}^{S}\left[L^2(Y_i)\right]^2}}$			
Learning Points	0.365343807	0.352414819	0.450915641
Verification Points	2.371328553	2.791127427	5.282166642
$L^2_{average-relative-error} = \frac{1}{S}\sum_{i=1}^{S} L^2_{relative-error}(Y_i)$			
Learning Points	0.38438512	0.353762951	0.537958322
Verification Points	2.558457076	3.188664815	6.118368823
$L^2_{\max-relative-error} = \max_{i=1\ldots S}\left[L^2_{relative-error}(Y_i)\right]$			
Learning Points	0.617910407	0.545968808	0.977039974
Verification Points	3.851450864	4.479913608	8.627830901
$L^\infty_{average-error} = \frac{1}{S}\sum_{i=1}^{S} L^\infty_{error}$			
Learning Points	1.121592313	31226.56506	1.483463997
Verification Points	3.151482851	153158.8556	29.03274379
$L^\infty_{\max-error} = \max_{i=1\ldots S}\left[L^\infty_{error}\right]$			
Learning Points	2.757662671	72891.43611	3.85019017
Verification Points	3.517435359	180510.1649	47.74508223

In Table 2, $L^2_{global\text{-}error}$ represents the relative global error associated with the L2 norm. The values were in the range of 0.35 to 0.45 % for learning points, and in the range of 2.37 to 5.28% for verification points. The $L^2_{average\text{-}relative\text{-}error}$ represents the mean relative error associated with the L2 norm. The range of values is similar to $L^2_{global\text{-}error}$. The $L^2_{max\text{-}relative\text{-}error}$ represents the maximum relative error associated with the L2 norm and is between 54 and 84% greater than $L^2_{average\text{-}relative\text{-}error}$ values.

Finally, $L^\infty_{average\text{-}error}$ and $L^\infty_{max\text{-}error}$ represent the average and maximum errors associated with the L∞. The dimensional nature of such errors must be emphasized.

It should be noted that the errors associated with the L2 norm in table 2 have 0% as the best value, while the errors associated with the L∞ norm have 0 as the best value.

4. CONCLUSION

Without being exhaustive, this work presents the ROM methodology applied to CFD simulation in a lab-scale stirred tank. For a range of defined input parameters, the ROM technique allows the generation of variable fields from a learning set of CFD simulations. The robustness of the technique was demonstrated: even for the small number of learning simulations the relative errors for the three fields were low. It should be noted that adding more learning points can further reduce errors associated with ROM predictions.

5. REFERENCES

Acar, E., 2010, Various approaches for constructing an ensemble of metamodels using local measures. *Structural and Multidisciplinary Optimization*, Vol. 42, n. 6, pp. 879-886.

Alexopoulos, A.H., Maggioris, D., and Kiparissides, C., 2002. CFD analysis of turbulence non-homogeneity in mixing vessels: A two-compartment model, *Chemical Engineering Science*, Vol. 57, Issue 10, pp. 1735-1752.

Almeida, P., and Costa, A.M.S., Souza, M., 2020. Direct and Indirect Optimization of CFD Experiments in Microfluidics: A Study of Case. In: *ENCIT 2020 - 18th Brazilian Congress of Thermal Sciences and Engineering*.

Antony, J., 2013. *Design of Experiments for Engineers and Scientists*, Elsevier.

Armenante, P.M., Luo, C., Chou, C.-C., and Fort, I., and Medek, J., 1997. Velocity profiles in a closed, unbaffled vessel: comparison between experimental LDV data and numerical CFD predictions, *Chemical Engineering Science*, Vol. 52, Issue 20, pp. 3483-3492.

Bakker, A., and Fasano, J.B, 1993 Time Dependent, Turbulent Mixing and Chemical Reaction in Stirred Tanks. In *Annual Aiche Meeting*, November 1993, St. Louis, Missouri, USA. AIChE Symposium Series 299, Vol. 90, pp. 71-78.

Ballarin, F., 2015. Reduced-order models for patient-specific haemodynamics of coronary artery bypass grafts. PhD thesis, Department of Mathematics, Politecnico di Milano.

Ballarin, F., Faggiano, E., Ippolito, S., Manzoni, A., Quarteroni, A., Rozza, G., and Scrofani, R. 2016. Fast simulations of patient-specific haemodynamics of coronary artery bypass grafts based on a POD – Galerkin method and a vascular shape parametrization. *Journal of Computational Physics*, Vol. 315, pp. 609–628.

Ben Salem, M., and Tomaso, L., 2018. Automatic selection for general surrogate models". *Structural and Multidisciplinary Optimization*, Vol. 58, n. 2, pp. 719-734.

Biancolini, M.E., Capellini, K., Costa, E., Groth, C., and Celi, S.X., 2020. Fast interactive CFD evaluation of hemodynamics assisted by RBF mesh morphing and reduced order models: the case of aTTA modeling. *International Journal on Interactive Design and Manufacturing*, Vol. 14, pp. 1227-1238.

Blais, B., and Bertrand, F., 2017. CFD-DEM investigation of viscous solid–liquid mixing: Impact of particle properties and mixer characteristics, *Chemical Engineering Research and Design*, Vol. 118, pp.270-285.

Brucato, A., Ciofalo, M., Grisafi, F., and Micale, G., 1998. Numerical prediction of flow fields in baffled stirred vessels: A comparison of alternative modelling approaches, *Chemical Engineering Science*, Vol. 53, Issue 21, pp. 3653-3684.

Carlberg, K., Farhat, C., Cortial, J., and Amsallem, D.,2013. The GNAT Method for Nonlinear Model Reduction: Effective Implementation and Application to Computational Fluid Dynamics and Turbulent Flows. *Journal of Computational Physics*, Vol. 242, pp. 623-647.

Chinesta, F., Keunings, R., and Leygue, A., 2014. *The Proper Generalized Decomposition for Advanced Numerical Simulations*. Springer International Publishing.

Haasdonk, B. and Ohlberger, M., 2008. Reduced basis method for finite volume approximations of parametrized linear evolution equations. Mathematical Modelling and Numerical Analysis, Vol. 42, Issue 2, pp. 277–302.

Han, S., Schirmer, C.M., and Modarres-Sadeghi, Y., 2020. A reduced-order model of a patient-specific cerebral aneurysm for rapid evaluation and treatment planning. *Journal of Biomechanics*, Vol. 103, 109653.

Hesthaven, J.S., Rozza, G., and Stamm, B. 2016. *Certified Reduced Basis Methods for Parametrized Partial Differential Equations*. Springer International Publishing.

Jung, S.K., Shin, S., Myong, R.S., and Cho, T.H., 2011. An efficient CFD-based method for aircraft icing simulation using a reduced-order model. *Journal of Mechanical Science and Technology*, Vol. 25, n. 3, pp. 703-711.

Kee, N.C.S., and Tan, R.B.H., 2002. CFD Simulation of Solids Suspension in Mixing Vessels, *The Canadian Journal of Chemical Engineering*, Vol. 80.

Lang, Y., Malacina, A., Bieler, L.T., Munteanu, S., Madsen, J.I., and Zitney, S.E., 2009. Reduced Order Model Based on Principal Component Analysis for Process Simulation and Optimization. *Energy & Fuels*, Vol. 23, pp. 1695-1706.

Laubenbacher, R., Sluka, J.P., and Glazier, J.A., 2021. Using digital twins in viral infection. Science, Vol. 371, 6534, pp. 1105-1106.

Maquart, T., Wenfeng, Y., Elguedj, T., Gravouil, A., and Rochette, M., 2020. 3D volumetric isotopological meshing for finite element and isogeometric based reduced order modeling. *Computer Methods in Applied Mechanics and Engineering*, Vol. 362, 112809.

Melinder, A., 2010. *Properties of Secondary Working Fluids for Indirect Systems*. International Institute of Refrigeration.

Montgomery, D.C., 2013. *Design and Analysis of Experiments*, Wiley.

Moro, F.R., 2016. *Estudo para a otimização de um impelidor de pás inclinadas em um tanque agitado através da Fluidodinâmica Computacional (CFD)* (in Portuguese). Master's Thesis, Graduate Program in Mechanical Engineering, Universidade Estadual de Maringá, Maringá, Brazil.

Myers, R.H., Montgomery, D.C., and Cook, and C.M., 2016. *Response Surface Methodology: Process and Product Optimization Using Design of Experiments*, Wiley.

Quarteroni, A. and Rozza, G., editors. 2014. Reduced Order Methods for Modeling and Computational Reduction, Vol. 9. Springer International Publishing.

Rodgers, T.L., Gangolf, L., Vannier, C., Parriaud, M., and Cooke, M., 2011. Mixing times for process vessels with aspect ratios greater than one, *Chemical Engineering Science*, Vol. 66, Issue 13, pp. 2935-2944.

Rozza, G., Malik, H., Demo, N., Tezzele M., Girfoglio, M., Stabile, G., and Mola, A., 2018. Advances in Reduced Order Methods for Parametric Industrial Problems in Computational Fluid Dynamics. *7th European Conference on Computational Fluid Dynamics*, Glasgow, UK.

Shekhar, S.M., and Jayanti, S., 2002. CFD Study of Power and Mixing Time for Paddle Mixing in Unbaffled Vessels, *Chemical Engineering Research and Design*, Vol. 80, Issue 5, pp. 482-498.

Stabile, G. and Rozza, G., 2018. Finite volume POD-Galerkin stabilised reduced order methods for the parametrised incompressible Navier-Stokes equations. *Computers & Fluids*.

Stabile, G., Hijazi, S., Mola, A., Lorenzi, S., and Rozza, G., 2017. PODGalerkin reduced order methods for CFD using Finite Volume Discretisation: vortex shedding around a circular cylinder. Communications in Applied and Industrial Mathematics, Vol. 8, Issue 1, pp. 210–236.

Tamburini, A., Cipollina, A., Micale, G., Brucato, A., and Ciofalo, M., 2014.Influence of drag and turbulence modelling on CFD predictions of solid liquid suspensions in stirred vessels, *Chemical Engineering Research and Design*, Vol. 92, Issue 6, pp. 1045-1063

Viana, F.A.C., Haftka, R.T., and Steffen, V., 2009. Multiple surrogates: How Cross-Validation Errors Can Help Us to Obtain the Best Predictor. *Structural and Multidisciplinary Optimization*, Vol. 39, n. 4, pp. 439-457.

Wadnerkar, D., Utikar, R.P., Tade, M.O., and Pareek. V.K., 2012. CFD simulation of solid–liquid stirred tanks, *Advanced Powder Technology*, Vol. 23, Issue 4, pp. 445-453.

Wang, S., Jiang, X., Wang, R., Xang, X., Yang, S., Zhao, J., and Liu, Y., 2017. Numerical simulation of flow behavior of particles in a liquid-solid stirred vessel with baffles, *Advanced Powder Technology*, Vol. 28, Issue 6, pp. 1611-1624.

Xiao, D., Fang, F., Buchan, A.G., Pain, C.C., Navon, I. M., and Muggeridge, A., 2015. Non-intrusive reduced order modelling of the Navier-Stokes equations. *Computer Methods in Applied Mechanics and Engineering*, Vol. 293, pp. 522-541.

Zhong, H., Xiong, Q., Yin, L., Zhang, J., Zhu, Y., Liang, S., Niu, B., and Zhang, X., 2020. CFD-based reduced-order modelling of fluidized-bed biomass fast pyrolysis using artificial neural network. *Renewable Energy*, Vol. 152, pp. 613-626.

6. RESPONSIBILITY NOTICE

The authors are the only responsible for the printed material included in this paper.